Hierarchically Ordered Nanoporous Pd/SBA-15 Catalyst for the Aerobic Selective Oxidation of Sterically Challenging Allylic Alcohols

7 AUTHORS, INCLUDING:

Christopher M. A. Parlett
Aston University
31 PUBLICATIONS **366** CITATIONS

SEE PROFILE

Karen Wilson
Aston University
235 PUBLICATIONS **5,169** CITATIONS

SEE PROFILE

Adam F Lee
Aston University
221 PUBLICATIONS **4,830** CITATIONS

SEE PROFILE

Hierarchically Ordered Nanoporous Pd/SBA-15 Catalyst for the Aerobic Selective Oxidation of Sterically Challenging Allylic Alcohols

Christopher M. A. Parlett,[†,⊥] Pooja Keshwalla,[†] Stephen G. Wainwright,[‡] Duncan W. Bruce,[‡] Nicole S. Hondow,[§] Karen Wilson,[†,∥] and Adam F. Lee*,[†,⊥,¶]

[†]Cardiff Catalysis Institute, School of Chemistry, Cardiff University, Cardiff CF10 3AT, U.K.
[‡]Department of Chemistry, University of York, Heslington, York YO10 4PF, U.K.
[§]Institute for Materials Research, University of Leeds, Leeds LS2 9JT, U.K.

⑤ *Supporting Information*

ABSTRACT: The utility of a hierarchically ordered nanoporous SBA-15 architecture, comprising 270 nm macropores and 5 nm mesopores (MM-SBA-15), for the catalytic aerobic selective oxidation of sterically challenging allylic alcohols is shown. Detailed bulk and surface characterization reveals that incorporation of complementary macropores into mesoporous SBA-15 enhances the dispersion of sub 2 nm Pd nanoparticles and thus their degree of surface oxidation. Kinetic profiling reveals a relationship between nanoparticle dispersion and oxidation rate, identifying surface PdO as the catalytically active phase. Hierarchical nanoporous Pd/MM-SBA-15 outperforms mesoporous analogues in allylic alcohol selective oxidation by (i) stabilizing PdO nanoparticles and (ii) dramatically improving in-pore diffusion and access to active sites by sesquiterpenoid substrates such as farnesol and phytol.
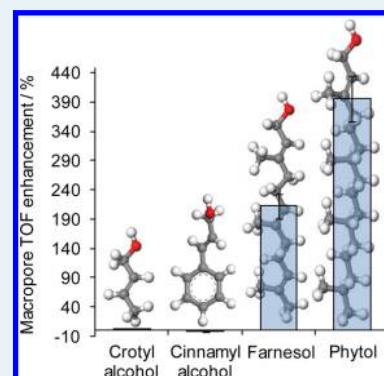
KEYWORDS: *palladium, selective oxidation, alcohol, hierarchical, macroporous, mesoporous, SBA-15*

INTRODUCTION

The aerobic selective oxidation (selox) of alcohols[1] represents an environmentally benign and atom-efficient chemical valorization route to commercially important allylic aldehydes, such as crotonaldehyde and cinnamaldehyde,[2] which find application in pesticides,[3] fragrances, and food additives.[4,5] Palladium nanoparticles are highly active and selective heterogeneous catalysts for such oxidative dehydrogenations,[1,6,7] permitting the use of air (or dioxygen) as a green oxidant in place of stoichiometric chromate[8] and permanganate salts[9] or H_2O_2.[10] Our recent operando,[11−13] in situ[14,15] and ex situ[16−19] spectroscopic studies on Pd nanoparticles have identified electron-deficient Pd(II), present as an atomically dispersed or extended surface PdO phase, as the catalytically active species in crotyl and cinnamyl alcohol selox, and highlighted on-stream reduction to palladium metal under oxygen poor regimes as the primary cause of deactivation. Despite this progress in the heterogeneously catalyzed selox of small alcohols and carbohydrates, no solid catalysts exist for the equivalent aerobic selox of long-chain/bulky alcohols such as phytol and farnesol, whose aldehydes are precursors to therapeutic acyclic sesquiterpenoids[20] employed in natural product synthesis.[21]

While attention has focused largely on the role of the metal component within Pd selox catalysts (and their Au–Pd,[22−24] Ru,[25,26] and Pt[27−29] analogues), the choice of support material can also influence reactivity. Commercial oxide and carbon supports have been employed widely in liquid phase selox

reactions;[30−33] however, custom-made surface chemical functionalization can confer benefits including: improved immobilization and dispersion of Pd over Schiff base[34] or PEG-treated silicas,[35] N-doped carbons,[36−38] tunable Pd particle size via acid (Al-doping)[39] or base (amino-silane grafting)[40] adjustment of silicas. Support morphology can also influence catalytic performance, wherein the introduction of mesoporosity into alumina dramatically enhanced Turnover Frequencies (TOFs) for the low temperature, Pd-catalyzed selox of crotyl, cinnamyl and benzyl alcohols.[17] Mesoporosity is also important for silica supported palladium nanoparticles, with three-dimensional interconnected SBA-16 and KIT-6 twice as active for crotyl and cinnamyl alcohol selox as comparable surface area two-dimensional SBA-15, which in turn outperforms amorphous silica.[18,19] Similar enhancements are reported for benzyl alcohol selox over mesoporous Pd/TUD-1.[40] We hypothesize that these differences reflect improved mass transport *and* the distribution of palladium nanoparticles created during catalyst synthesis, with site isolation in an ordered nanoporous matrix stabilizing smaller particles with a higher degree in the active PdO form. With this in mind, it is interesting to consider the impact of coupling a secondary, macropore skeleton with a mesoporous network upon Pd catalyzed selox of small and long-chain allylic alcohols.

The first such ordered, hierarchical macroporous-mesoporous (MM) solid was only reported in 1998,[41] unlocking a versatile means to improve mesopore accessibility; secondary macropores can be envisaged as "superhighways" that funnel gas/liquid flow into the high surface area mesopores. While scientific interest in the synthesis of hierarchical MM materials has grown rapidly,[42,43] to date there have been few examples of their application within heterogeneous catalysis. MM TiO_2/SiO_2 and TiO_2/ZrO_2 nanocomposites have been exploited for their enhanced light harvesting properties in photocatalysis,[44] while Fe_2O_3,[45] SiCN,[46] and alumina[47] analogues have been employed in gas-phase Fischer–Tropsch synthesis, methane combustion, and CO oxidation, respectively. Ordered, hierarchical sulfonic acid SBA-15 and MgAl hydrotalcite variants have also been employed to promote liquid-phase biodiesel production from viscous bio-oils,[24,48] and the benefit of macropores noted in α-olefin epoxidation by TBHP over a Ti-substituted, hierarchical MM silica.[49]

Here we report the first use of an ordered MM catalyst support, namely, MM-SBA-15, for the catalytic oxidation of alcohols. This hierarchical support material has been evaluated alongside a conventionally synthesized Pd/SBA-15 (which contains ordered mesopores and random micropores), and one produced via a true liquid crystal templating methodology (Pd/TLCT-SBA-15) with reduced microporosity. We reveal how the hierarchical support architecture confers significant advantages in terms of (i) enhanced Pd dispersion/surface oxidation over mesoporous counterparts, and thus promoted crotyl and cinnamyl alcohol selox; and (ii) unlocking the sterically challenging aerobic selox of long-chain substrates like farnesol and phytol.

■ EXPERIMENTAL SECTION

MM-SBA-15 was produced via the method of Dhainaut et al.,[24] using Pluronic P123 and polystyrene microspheres as respective meso- and macropore directing agents. Pluronic P123 was also used to prepare SBA-15 via the method reported by Zhao et al.,[50] and TLCT-SBA-15 by templating on the preformed mesophase of P123.[51] Aqueous incipient-wetness impregnation of each support with tetraamine palladium(II) nitrate, followed by calcination and reduction, allowed for the preparation of three families of Pd/silicas with nominal loadings spanning 0.05–5 wt %.

The following chemicals were employed without further purification: potassium persulfate (Sigma Aldrich ≥99%), Styrene (Sigma Aldrich ≥99%), divinylbenzene (Sigma Aldrich 80%), sodium hydroxide pellets (Fisher 99%), ethanol (Fisher ≥99.8%), pluronic P123 (Sigma Aldrich), hydrochloric acid (Fisher 32%), tetramethoxysilane (Sigma Aldrich 98%), tetraamine palladium(II) nitrate solution (Sigma Aldrich 99.99% 10 wt %), crotyl alcohol (Sigma Aldrich 96%), cinnamyl alcohol (Sigma Aldrich 98%), farnesol (Sigma Aldrich 95%), phytol (Sigma Aldrich ≥97%), toluene (Fisher ≥99%), and mesitylene (Acros 99%).

Polystyrene Microsphere Synthesis. Potassium persulfate (0.16 g) was dissolved in distilled water (12 cm^3) at 70 °C. In a separate 500 cm^3 three-necked round bottomed flask, distilled water (377 cm^3) was purged under N_2 (10 cm^3 min^{-1}) at 70 °C. Styrene (50 cm^3) and divinylbenzene (9.5 cm^3) were each washed three times with sodium hydroxide solution (0.1 M, 1:1 vol/vol) followed by three washings with distilled water (1:1 vol/vol) to remove polymerization inhibitors. The washed organic phases were then added to the purged water phase

followed by the potassium persulfate solution. The mixture was left to stir under flowing nitrogen (10 cm^3 min^{-1}) for 15 h, and the resulting microspheres filtered and washed three times with distilled water (100 cm^3) and then three times with ethanol (100 cm^3).

MM-SBA-15 Synthesis. Pluronic P123 (10 g) was dissolved in water (75 cm^3) and hydrochloric acid (2 M, 290 cm^3) with stirring at 35 °C. Polystyrene microspheres (45 g) were added, and the solution stirred for 1 h. Tetramethoxysilane (15.0 cm^3) was then added and left for 20 h with agitation. The resulting gel was aged in a sealed polyethylene bottle for 24 h at 80 °C under static conditions. The solid was filtered, washed with water (1000 cm^3), and dried at room temperature before calcination at 550 °C for 6 h in air (ramp rate 0.5 °C min^{-1}).

SBA-15 Synthesis. Pluronic P123 (10 g) was dissolved in water (75.5 cm^3) and hydrochloric acid (2 M 291.5 cm^3) with stirring at 35 °C. Tetramethoxysilane (15.5 cm^3) was added and left for 20 h with agitation. The resulting gel was aged in a sealed polyethylene bottle for 24 h at 80 °C without agitation. The solid was filtered, washed with water (1000 cm^3), and dried at room temperature before calcination at 500 °C for 6 h in air (ramp rate 1 °C min^{-1}).

TLCT-SBA-15 Synthesis. Pluronic P123 (0.5 g) was mixed with hydrochloric acid acidified water (pH = 2, 0.5 g) and sonicated at 40 °C to produce a homogeneous gel. Tetramethoxysilane (1.02 cm^3) was added and mixed to form a homogeneous liquid. The evolved methanol was removed under a light vacuum (0.12 bar) at 40 °C to form a viscous gel. The gel was exposed to the atmosphere at room temperature for 24 h to complete condensation before calcination at 500 °C for 6 h in air (ramp rate 3 °C min^{-1}).

Palladium Impregnation. MM-SBA-15 (1.0 g) was wetted with aqueous tetraamine palladium(II) nitrate solution (10 cm^3) with nitrate precursor concentrations adjusted to achieve nominal Pd loadings of 0.05–2.5 wt %. SBA-15 and TLCT-SBA-15 (1.5 g) were likewise wetted with aqueous tetraamine palladium(II) nitrate solution (12 cm^3) with nitrate precursor concentrations adjusted to achieve nominal Pd loadings of 0.05–5 wt %. Resulting slurries were stirred for 18 h at room temperature before heating to 50 °C. Agitation was ceased after 5 h, and the solids left at 50 °C for 24 h to dry to a powder. These powders were calcined at 500 °C for 2 h in air (ramp rate 1 °C min^{-1}), then cooled to room temperature and subjected to a second high temperature treatment at 400 °C (ramp rate 10 °C min^{-1}) for 2 h under flowing hydrogen (10 cm^3 min^{-1}), cooled and stored under ambient conditions.

Characterization. Nitrogen porosimetry was undertaken on a Quantachrome Nova 1200 porosimeter, and data analyzed using NovaWin 2 version 2.2 software. Samples were degassed at 120 °C for 2 h prior to analysis at −196 °C. Adsorption/desorption isotherms were recorded for all parent and Pd-impregnated silicas. Brunauer–Emmett–Teller (BET) surface areas were calculated over the relative pressure range 0.01–0.2, with micropore surface area assessed using the t-plot methodology over the relative pressure range 0.2–0.5. Pore diameters and volumes were calculated applying the Barret–Joyner–Halenda (BJH) method to the desorption isotherm for relative pressures >0.35. Low and wide angle X-ray diffraction (XRD) patterns were recorded on a PANalytical X'pertPro diffractometer fitted with an X'celerator detector and Cu K_α (1.54 Å) source with calibration against a Si standard. Low angle patterns were recorded for 2θ = 0.3–8° with a step size of 0.01°. Wide

angle patterns were recorded for $2\theta = 25-75°$ with a step size of 0.02°. The Scherrer equation was used to calculate volume-averaged Pd particle sizes. High resolution (scanning) transmission electron microscopy ((S)TEM) images were recorded on an FEI Tecnai F20 field emission gun TEM operating at 200 kV equipped with a Gatan Orius SC600A CCD camera. Samples were prepared by dispersing in methanol and drop-casting onto a copper grid coated with a holey carbon support film (Agar Scientific Ltd.). Images were analyzed in ImageJ 1.41. Scanning electron microscopy (SEM) images were recorded on a Carl Zeiss Evo-40 SEM operating at 10 kV. Samples were mounted on aluminum stubs using adhesive carbon tape and gold splutter coated to reduce charging. X-ray photoelectron spectroscopy (XPS) was performed on a Kratos Axis HSi X-ray photoelectron spectrometer fitted with a charge neutralizer and magnetic focusing lens employing Al K_α monochromated radiation (1486.6 eV). Spectral fitting was performed using CasaXPS version 2.3.14. Binding energies were corrected to the Si 2p peak at 103.4 eV. Pd 3d XP spectra were fitted using a common asymmetric peak shape determined from palladium oxide standard. Errors were estimated by varying the Shirley background-subtraction procedure across reasonable limits and recalculating the component fits. Pd loadings were determined by MEDAC Analytical and Chemical Consultancy Service Ltd. Samples were digested in hydrofluoric acid prior to ICP analysis on a Varian Vista-MPX ICP optical emission spectrometer. Pd metal surface areas were measured via CO pulse chemisorption on a Quantachrome ChemBET 3000 system, assuming a Pd:CO stoichiometry of 1:2.[52] Samples were outgassed at 150 °C under flowing He (20 cm^3 min^{-1}) for 1 h, prior to reduction at 100 °C under flowing hydrogen (20 cm^3 min^{-1}) for 1 h before analysis at room temperature. Note, this reduction protocol is milder than that employed during Pd impregnation, and thus does not induce additional particle sintering.

Aerobic Selective Alcohol Oxidation. Catalyst screening was performed using a Radleys Starfish carousel batch reactor on a 10 cm^3 scale at 90 °C under atmospheric pressure of air. Catalysts (50 mg for crotyl and cinnamyl alcohol, unless stated otherwise, and 200 mg for farnesol and phytol) were added to reaction mixtures containing either 8.4 mmol of crotyl or cinnamyl alcohol, or 4.2 mmol of farnesol or phytol, an internal standard (mesitylene, 0.1 cm^3), and 10 cm^3 of toluene solvent at 90 °C under stirring. The absolute Pd level varied between 0.47 μmol (0.05 wt % catalysts) and 23.0 μmol (for the highest loading 4.89 wt % Pd/TLCT-SBA-15 tested), corresponding to substrate:catalyst mol ratios ranging from 17,872 down to 365. Reactions were sampled periodically for kinetic and selectivity profiling by off-line gas chromatography using a Varian 3900GC with 8400 autosampler fitted with a (15 m × 0.25 mm × 0.25 μm) CP-Sil5 CB column, which had been multipoint calibrated to reactant alcohols and products including crotonaldehyde, butanal, cinnamaldehyde, cinnamic acid, 3-phenyl-1-propanol, 3-phenylpropanal, 3-phenylpropanoic acid, trans-β-methylstyrene, styrene, and ethylbenzene. Phytol and farnesol reaction profiling and product selectivities were assessed by off-line GC-MS using an Agilent 220 ion-trap GC-MS with 8400 autosampler fitted with a (25 m × 0.25 mm × 0.25 μm) CP-Sil5 CB column.

■ RESULTS AND DISCUSSION

Successful synthesis of an ordered macroporous skeleton for the MM-SBA-15 support was confirmed by SEM and TEM in

Figure 1. These revealed monodispersed, regularly packed macropores with mean diameters between 260 and 280 nm
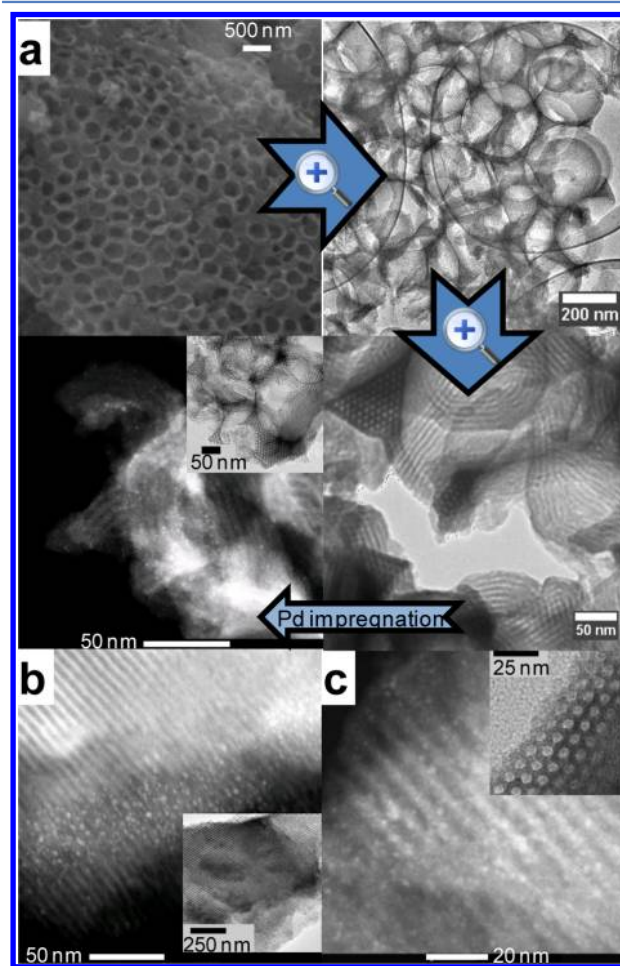

Figure 1. SEM, TEM, and HAADF-STEM images of (a) parent and 0.78 wt % Pd/MM-SBA-15; (b) 0.46 wt % Pd/TLCT-SBA-15; and (c) 0.89 wt % Pd/SBA-15. Bright-field TEM micrographs for the conventional mesopore supports are shown inset.

(consistent with the 270 nm polystyrene template). In contrast, SBA-15 exhibited the expected straw-like morphology,[53] while TLCT-SBA-15 comprised larger angular crystallites, spanning a wide size distribution (Supporting Information, Figure S1). Genesis of a mesoporous SBA-15 framework permeating all three silica supports was evidenced by TEM, low-angle powder XRD, and porosimetry, with ordered hexagonal (*p6mm*) arrangements of monodispersed, uniform mesopores observed in all cases (Figures 1−2 and Supporting Information, Figure S2). Associated textural properties are reported in Table 1. BET surface areas for the parent MM-SBA-15 and TLCT-SBA-15 supports were both ~550 m^2 g^{-1}, significantly lower than for SBA-15 because of the latter's greater (random) microporosity. The TLCT route may disfavor microporosity because of the rapid condensation of silica walls, as observed during evaporation-induced self-assembly.[54] The BJH pore diameters of MM-SBA-15 and TLCT-SBA-15 are somewhat smaller than those of SBA-15, mirroring their contracted XRD-derived mesopore unit cell dimensions. This may reflect lack of a hydrothermal treatment step for TLCT-SBA-15, which can induce pore and unit cell expansion,[50] and a limited "hydrothermal effect" for MM-SBA-15 imposed by silica
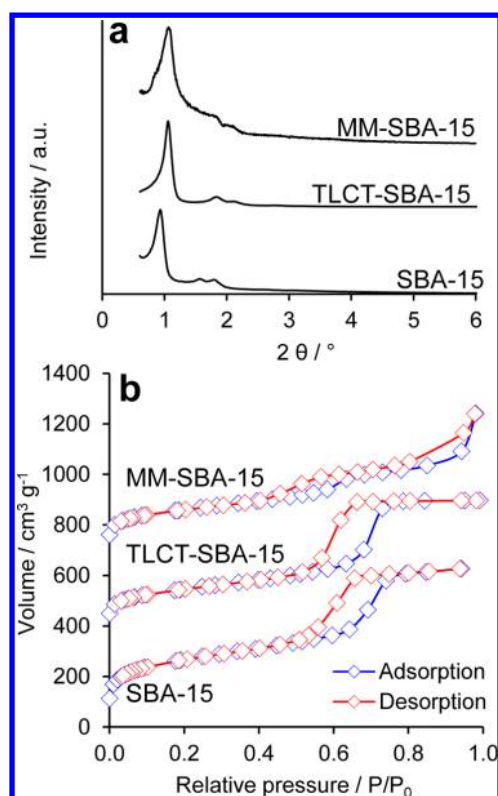
Figure 2. (a) Low angle XRD patterns of silica supports (note weaker reflections due to macropore disruption of the mesopore domains); (b) corresponding N_2 isotherms (offset by 700 and 400 cm^3 g^{-1} for MCM-SBA-15 and TLCT-SBA-15, respectively).

Table 1. Physical Properties of Parent Silica Supports

support	surface area^a (m^2 g^{-1}) (nm)	mesopore diameter^b (nm)	mesopore unit cell^c (nm)
MM-SBA-15	570 (190)	3.8	7.2
TLCT-SBA-15	530 (100)	5.1	7.3
SBA-15	950 (460)	5.7	9.4

^{a}BET value with t-plot micropore surface area in parentheses. ^{b}BJH value. ^{c}Determined from low-angle XRD.

confinement at the periphery of macropore voids, which furthermore constrains the overall length of mesopore channels within this hierarchical silica.

Low-angle XRD, N_2 porosimetry, and bright/dark field (S)TEM confirmed the retention of ordered SBA-15 mesopore networks upon Pd impregnation for all three supports (Figure 1 and Supporting Information, Figure S3), with negligible change in mesopore unit cells or pore diameters (Supporting Information, Figure S4). However, corresponding BET surface areas fell with rising bulk palladium loading (Figure 3), reflecting lost microporosity, either through micropore filling or capping by Pd nanoparticles. This loss was greatest for Pd/SBA-15 wherein the parent silica possessed the highest micropore area. Mesopores remained unaffected, with >95% of the initial mesopore surface areas retained, indicating that Pd clusters were smaller than the mesopore dimensions in all three silicas. This conclusion was supported by the absence of crystalline palladium phases in wide-angle XRD patterns for any Pd/MM-SBA-15 samples, consistent with the presence of highly dispersed (<2 nm) nanoparticles. Although fcc Pd particles were observed at the highest loadings over the other
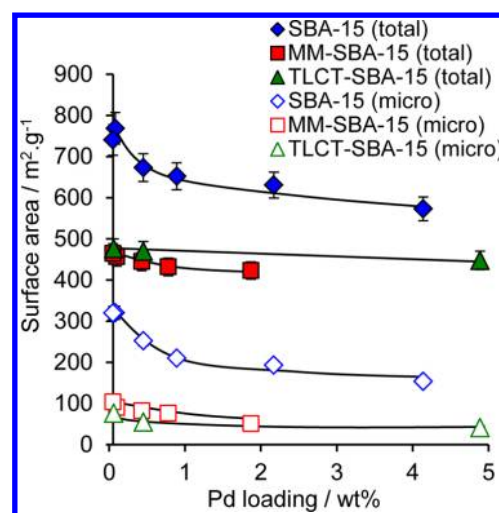

Figure 3. Influence of Pd loading upon total (BET) and micropore surface areas (determined by t-plot analysis).

supports, the resulting volume-averaged diameters of 3.4 nm (4.89 wt % Pd/TLCT-SBA-15) and 2.8 nm (4.14 wt % Pd/SBA-15) determined via Scherrer analysis (Supporting Information, Figure S5) were still significantly smaller than the mean mesopores. HAADF-STEM images in Figure 1 reveal Pd nanoparticles as uniformly distributed bright spots within the mesopores of MM-SBA-15 and SBA-15 supports, whereas these appear clustered at the perimeter (and possibly pore entrances) of the TLCT-SBA-15 support.

Table 2 summarizes the properties of the silica supported palladium nanoparticles, highlighting a strong correlation

Table 2. Properties of Silica Supported Pd Nanoparticles

support	Pd loading^a (wt %)	dispersion^b (%)	particle size^b (nm)	surface PdO^c (%)
MM-SBA-15	1.87	62	1.8	5.0
MM-SBA-15	0.78	68	1.6	8.7
MM-SBA-15	0.43	71	1.6	12.8
MM-SBA-15	0.10	78	1.4	25.8
MM-SBA-15	0.05	83	1.2	30.2
TLCT-SBA-15	4.89	32	3.0	1.6
TLCT-SBA-15	0.46	54	2.1	5.0
TLCT-SBA-15	0.06	72	1.5	12.1
SBA-15	4.14	3	2.9	2.1
SBA-15	2.17	43	2.6	3.3
SBA-15	0.89	52	2.3	5.1
SBA-15	0.45	56	1.9	7.1
SBA-15	0.08	64	1.7	13.3
SBA-15	0.05	78	1.4	18.3

^{a}ICP-MS analysis. ^{b}Dispersion and particle size estimated from CO chemisorption. ^{c}Determined from fitted Pd 3d XP spectra.

between Pd loading and particle size for all supports. Mean nanoparticle sizes determined by CO chemisorption were significantly smaller than the mesopore dimensions in accordance with wide angle XRD. For any chosen metal loading, incorporation of the secondary macropore network resulted in smaller nanoparticles, that is, high dispersions, which recalling the higher BET surface area of the conventional SBA-15 support, evidence more efficient use of the mesopore network within the hierarchical MM-SBA-15 architecture during Pd impregnation. It is noteworthy that the Pd/TLCT-

SBA-15 family, which lacks either the ordered macropores of Pd/MM-SBA-15 or the random micropores of Pd/SBA-15 families, exhibited the poorest dispersions. In addition to lacking complementary macroporosity, the TLCT-SBA-15 support also possesses far longer (up to 1–2 μm) mesopore channels, which may hinder the uniform distribution of Pd during impregnation, and promote sintering during subsequent thermochemical processing. This hypothesis is consistent with the localized band of larger Pd nanoparticles visualized by HAADF-STEM in Figure 1b.

We previously identified a strong dependence of Pd surface oxidation state (both ex situ[16−19] and in situ[55]) on particle dispersion over amorphous and mesoporous aluminas and silicas. Figure 4 shows that this relationship between surface
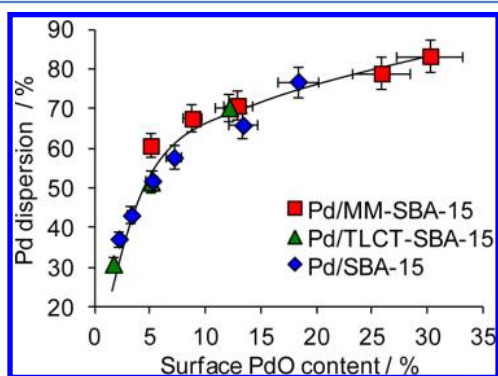
Figure 4. Relationship between surface PdO concentration and dispersion across mesoporous and hierarchical silicas.

PdO concentration and dispersion (derived from Pd 3d XP spectra in Supporting Information, Figure S6) is indeed a general phenomenon for "nonreducible" silica supports, irrespective of their morphology. This is a key discovery, as it demonstrates that for such weakly interacting supports, palladium surface oxidation is entirely dispersion-controlled, and hence tunable through judicious choice of support architecture and metal loading. Geometric modeling of an oxide shell-metal core nanoparticle suggests that the initial linear rise in oxide content with dispersion is consistent with a constant, small (∼5%) fractional surface oxide coverage for particles between 1.5 and 3 nm diameter. As particle diameters fall below 1.5 nm, even small increases in dispersion >60% induce a sharp rise in the fraction of palladium atoms within the outermost few atomic layers, with oxide versus metal surface energies dictating a consequent rapid rise in the degree of surface oxidation.

The impact of these textural and compositional changes upon catalytic reactivity was assessed for Pd/MM-SBA-15 in the liquid phase aerobic selox of crotyl and cinnamyl alcohols (reaction profiles shown in Supporting Information, Figures S7 and S8) in the absence of external mass transport limitations (Supporting Information, Figure S9). Quantitative benchmarking of mass normalized initial rates against mesoporous Pd/SBA-15 and Pd/TLCT-SBA-15 is presented in Figure 5. An inverse relationship between bulk Pd loading and activity was observed for all three supports, akin to that recently reported over KIT-6 and SBA-16 interconnected, mesoporous silicas.[16,19] However, the hierarchical Pd/MM-SBA-15 catalysts significantly outperform the conventional mesoporous SBA-15 by 30−50% for both alcohols, while the Pd/TLCT-SBA-15 is proportionately poorer. This rate enhancement is such that Pd/
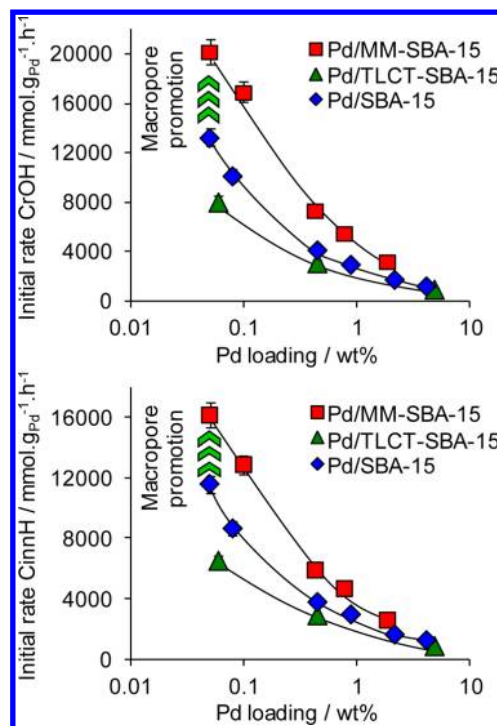
Figure 5. Dependence of (*top*) crotyl and (*bottom*) cinnamyl alcohol aerobic selox activity on Pd loading and support nature.

MM-SBA-15 catalysts exhibit comparable activity to palladium dispersed on the higher area, three-dimensional SBA-16 and KIT-6 architectures.[18,19] We postulate that by truncating the long, parallel mesopore channels formed in typical SBA-15 syntheses, macropores facilitate more uniform deposition of the palladium precursor throughout the entire mesopore network, thus hampering subsequent sintering and concomitant reduction to metallic Pd during catalyst pretreatment and use. The order of activity, MM-SBA-15 > SBA-15 > TLCT-SBA-15 correlates with the initial surface PdO content, (Table 2), as anticipated for the proposed Pd(II) active species.

TOFs for the hierarchical and mesoporous Pd/silicas, obtained by normalizing the preceding initial selox rates per mole of surface PdO (from XPS) or surface Pd metal (from CO chemisorption), are shown in Figure 6. These evidence a common surface PdO phase as the active species in both crotyl and cinnamyl alcohol selox. This conclusion is in accordance with in situ XAS[55] and ambient pressure XPS[15] studies of crotyl alcohol selox over Pd nanoparticles and Pd(111) model catalysts, which show that crotyl alcohol conversion is proportional to the PdO content *measured during reaction*, with Pd_5O_4/Pd(111) and PdO/Pd(111) surfaces exposed to a flowing mixture of 1 mTorr crotyl alcohol and 140 mTorr O_2 sustaining crotonaldehyde production whereas metallic Pd(111) is unreactive. In situ reduction of PdO nanoparticles supported on a KIT-6 mesoporous silica was recently seen to poison their activity and selectivity in cinnamyl alcohol selox,[18] a process that was partially reversible under high oxygen partial pressures. Such observations provide definitive proof that surface palladium oxide is indeed the active phase in allylic alcohol selox as advanced herein.

Observation of a constant TOF, independent of support architecture, for these small allylic alcohols also provides convincing evidence that in-pore diffusion is not rate-limiting under our conditions. This suggests that the loss of
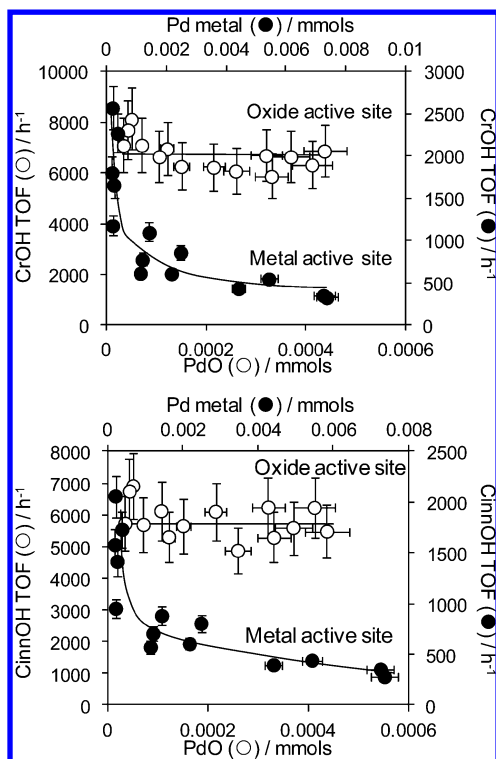
Figure 6. Crotyl (*top*) and cinnamyl (*bottom*) alcohol aerobic selox TOFs as a function of surface PdO or Pd metal content for Pd/MM-SBA-15, Pd/TLCT-SBA-15, and Pd/SBA-15 catalysts.
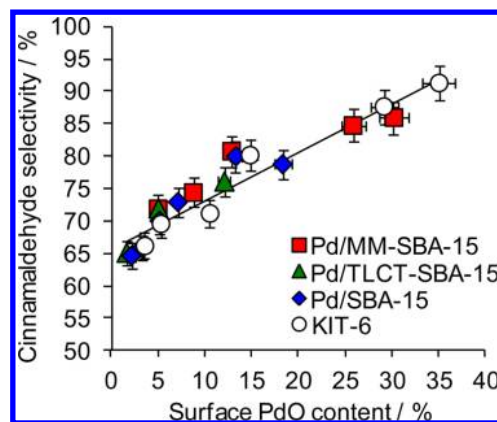

Figure 7. Linear relationship between initial selox selectivity to cinnamaldehyde and surface PdO concentration. Excellent agreement is observed with previously reported data on Pd/KIT-6.[18]

Figure 8 shows that farnesol and phytol conversion are strongly promoted over 0.43 wt % Pd/MM-SBA-15 versus 0.45 wt %
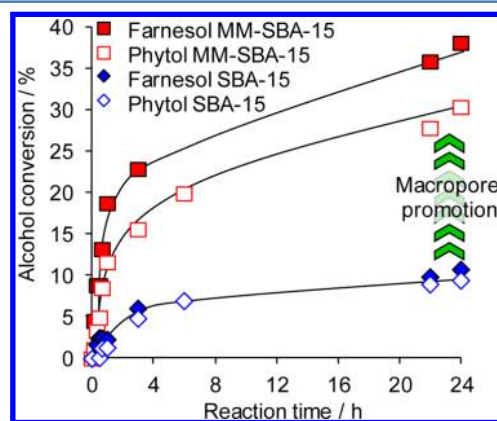

Figure 8. Impact of macroporosity on the aerobic selox of farnesol and phytol over Pd/MM-SBA-15 versus Pd/SBA-15.

microporosity in Figure 3 following palladium impregnation does not arise from significant Pd nanoparticles forming within the micropores, but rather micropore capping by easily accessible nanoparticles residing within the mesopore/macropore channels. The absolute TOFs of 5,900 h^{-1} (cinnamyl) and 6,800 h^{-1} (crotyl) for all three catalyst families are in excellent agreement with those from Pd impregnated amorphous silica, KIT-6 and SBA-16.[19]

Crotonaldehyde and cinnamaldehyde were the major products over the hierarchical and mesoporous SBA-15 supports (Supporting Information, Figure S10), with 24 h selectivities of ~60−70%, comparable to literature values under similar mild aerobic conditions.[6] However, initial cinnamaldehyde selectivity values evaluated between 10 and 20 min reaction and low conversions (<10%) were far superior. For all catalysts, a linear relationship between initial aldehyde selectivity and surface PdO content of the as-prepared materials was evident (Figure 7), highlighting the importance of Pd(II) species in achieving both high selox activity *and* aldehyde yields. This is explicable in terms of the other minor products observed, which predominantly arose through competing C═ C hydrogenation, via surface hydrogen liberated during the initial alcohol activation step,[6] and decarbonylation steps, reactions strongly favored by reduced Pd(0) metal surfaces.[15,56] For any given Pd loading, the MM-SBA-15 support conferred greater selectivity to cinnamaldehyde than the higher area SBA-15 silica, in line with the former's enhanced ability to stabilize palladium oxide.

An even more striking demonstration of the benefits of macropore incorporation into hierarchical frameworks is provided by the aerobic selox of farnesol (C$_{15}$) and phytol (C$_{20}$). These substrates are substantially bulkier than crotyl and cinnamyl alcohols, with molecular diameters of ~1.5−2 nm.

Pd/SBA-15, with the latter exhibiting poor conversions even after 24 h. The dramatic impact of macropores upon activity toward these larger allylic alcohols is even more apparent upon comparing the initial selox rates and TOFs across all four alcohols (Figure 9). In Figure 5 we noted that macropores substantially accelerated both crotyl and cinnamyl alcohol selox initial rates relative to a conventional Pd/SBA-15; however, such rate enhancements pale by comparison to those observed for farnesol (420%) and phytol (720%). The analogous TOF comparison is even more illuminating. A common value is observed for the smaller alcohols, independent of macropores, precisely as anticipated if oxidation of these substrates proceeds without diffusion limitations over identical types of (surface PdO) species within both catalysts. In contrast, the TOFs for farnesol and phytol (respectively 480 h^{-1} vs 1502 h^{-1} and 252 h^{-1} vs 1258 h^{-1}) reveal huge rate enhancements upon macropore introduction, evidencing the elimination of mass-transport barriers inherent in SBA-15 and thus vastly improved accessibility to mesopores wherein the overwhelming majority of PdO nanoparticles reside (macropores accounting for <2% of the total surface area).

Our hypothesis that a critical function of macropores is to improve in-pore molecular diffusion of bulky alcohols is supported by comparing the apparent activation energies for
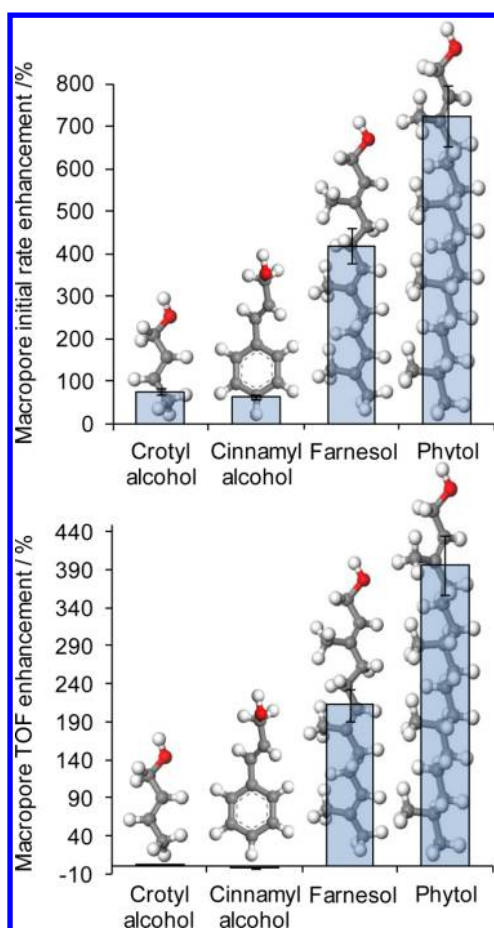
Figure 9. Macropore enhancement of (*top*) initial rates and (*bottom*) TOFs over 0.43 wt % Pd/MM-SBA-15 versus 0.45 wt % Pd/SBA-15.

farnesol and cinnamyl alcohol selox over 0.43 wt % Pd/SBA-15 versus 0.45 wt % Pd/MM-SBA-15. For temperatures between 80 and 100 °C, $\Delta E_{act}^{farnesol}$ was only 12 ± 5 kJ mol^{-1} for the Pd/SBA-15 catalyst, versus 38 ± 5 kJ mol^{-1} for the equivalent hierarchical Pd/MM-SBA-15. This observation of a significantly lower $\Delta E_{act}^{farnesol}$ for the mesoporous support is in line with expectations for a diffusion rate-limited reaction. The higher value for the MM silica is similar to that reported for aerobic selox of (the smaller) crotyl alcohol over comparable loading Pd/meso-Al$_2$O$_3$ catalysts,[17] wherein negligible diffusion barriers are anticipated, which span 37−45 kJ mol^{-1}. By way of contrast, there is little difference between $\Delta E_{act}^{cinnamyl\ alcohol}$ over Pd/SBA-15 and Pd/MM-SBA-15, which at 46 and 41 kJ mol^{-1} respectively are consistent with a reaction rate-limited oxidation. Hence small differences in the static kinetic diameters of farnesol (∼0.45 nm) and phytol (∼0.54 nm) determined via density functional theory (DFT) calculations (Supporting Information, Figure S11) and cinnamyl alcohol (∼0.3 nm), coupled with the higher molecular weight and greater flexibility and dynamic motion associated with the longer hydrocarbon backbones of the sesquiterpenoids, appear sufficient to hamper transport of bulky alcohols necessitating complementary macroporosity.

■ CONCLUSIONS

We have demonstrated the first synthesis of a hierarchically ordered, MM Pd/silica catalyst, and demonstrated its efficiency in the aerobic selox of allylic alcohols to their aldehydes.

Macropore incorporation into a mesoporous SBA-15 framework enhances subsequent dispersion (and attendant surface oxidation) of Pd nanoparticles located in-pore via postsynthetic wet impregnation; this may reflect more uniform intrusion of the palladium precursor throughout the mesopore channels, and fracturing of mesopores to limit their length and thus restrict nanoparticle migration and concomitant sintering and reduction during thermochemical processing.

A strong relationship between nanoparticle dispersion and corresponding activity toward crotyl and cinnamyl alcohol aerobic selox was observed for hierarchical Pd/MM-SBA-15 catalysts, mirroring that of mesoporous Pd/silica and alumina analogues, suggesting an origin in the atomic scale properties of palladium nanoparticles (oxidation state) and not the support architecture. Absolute crotyl and cinnamyl alcohol selox rates of Pd/MM-SBA-15 catalysts were superior to those for equivalent Pd loadings on mesoporous SBA-15, irrespective of whether micropores were present within the latter support. However, since the hierarchical and purely mesoporous supports exhibited identical TOFs toward each of these small alcohols, these selox rate enhancements do not reflect differential in-pore diffusion, but the greater stabilization of PdO over MM-SBA-15. This contrasts with the case of long chain allylic alcohols, wherein the excellent selox activity of Pd/MM-SBA-15 arises from the combination of enhanced palladium dispersion *and accessibility of active surface PdO sites* (evidenced by the greatly increased TOFs with respect to mesoporous Pd/SBA-15). The latter factor is critical to achieving the first reported aerobic oxidation of farnesol or phytol by a heterogeneous catalyst. In summary, an efficient palladium-derived selox catalyst requires support materials which possess two key properties: the ability to disperse and stabilize high concentrations of PdO within the surface of <2 nm particles; large pore channels to minimize mass-transport limitations in supplying alcohol substrate and oxygen to active sites and returning aldehyde product to the bulk reaction media. We are exploring hierarchically porous reducible metal oxide supports as next-generation candidates to tailor both these properties.

Further development of such ordered hierarchical nanoporous architectures may pave the way to the undertaking of complex organic synthetic transformations, especially those pertinent to natural product synthesis, over solid state catalysts under greener reaction conditions.

■ ASSOCIATED CONTENT

ⓢ Supporting Information

Additional support and catalyst characterization, and selox reaction data. This material is available free of charge via the Internet at http://pubs.acs.org.

■ AUTHOR INFORMATION

Corresponding Author

*E-mail: leeaf@cardiff.ac.uk, a.f.lee@warwick.ac.uk.

Present Addresses

[⊥]Department of Chemistry, University of Warwick, Coventry, CV4 7AL, U.K.

[‖]European Bioenergy Research Institute, School of Engineering and Applied Science, Aston University, Birmingham, B4 7ET, U.K.

[¶]School of Chemistry, Monash University, Victoria 3800, Australia

Notes

ABBREVIATIONS

BET, Brunauer−Emmett−Teller equation; BJH, Barret−Joyner−Halenda calculation; ICP, Inductive coupled plasma; CrotOH, Crotyl alcohol; CinnOH, Cinnamyl alcohol

REFERENCES

(1) Vinod, C. P.; Wilson, K.; Lee, A. F. *J. Chem. Technol. Biotechnol.* **2011**, *86*, 161.

(2) Uozumi, Y.; Yamada, Y. M. A. *Chem. Rec.* **2009**, *9*, 51.

(3) Cheng, S. S.; Liu, J. Y.; Tsai, K. H.; Chen, W. J.; Chang, S. T. *J. Agric. Food Chem.* **2004**, *52*, 4395.

(4) Brul, S.; Coote, P. *Int. J. Food Microbiol.* **1999**, *50*, 1.

(5) Cocchiara, J.; Letizia, C. S.; Lalko, J.; Lapczynski, A.; Api, A. M. *Food Chem. Toxicol.* **2005**, *43*, 867.

(6) Mallat, T.; Baiker, A. *Chem. Rev.* **2004**, *104*, 3037.

(7) Dimitratos, N.; Lopez-Sanchez, J. A.; Hutchings, G. J. *Chem. Sci.* **2012**, *3*, 20.

(8) Lee, D. G.; Spitzer, U. A. *J. Org. Chem.* **1970**, *35*, 3589.

(9) Prabhakaran, P. V.; Venkatachalam, S.; Ninan, K. N. *Eur. Polym. J.* **1999**, *35*, 1743.

(10) Sheldon, R. A.; Arends, I.; Dijksman, A. *Catal. Today* **2000**, *57*, 157.

(11) Lee, A. F.; Wilson, K. *Green Chem.* **2004**, *6*, 37.

(12) Parlett, C. M. A.; Gaskell, C. V.; Naughton, J. N.; Newton, M. A.; Wilson, K.; Lee, A. F. *Catal. Today* **2013**, *205*, 76.

(13) Lee, A. F.; Ellis, C. V.; Naughton, J. N.; Newton, M. A.; Parlett, C. M. A.; Wilson, K. *J. Am. Chem. Soc.* **2011**, *133*, 5724.

(14) Lee, A. F.; Chang, Z.; Ellis, P.; Hackett, S. F. J.; Wilson, K. *J. Phys. Chem. C* **2007**, *111*, 18844.

(15) Lee, A. F.; Naughton, J. N.; Liu, Z.; Wilson, K. *ACS Catal.* **2012**, *2*, 2235.

(16) Lee, A. F.; Hackett, S. F. J.; Hargreaves, J. S. J.; Wilson, K. *Green Chem.* **2006**, *8*, 549.

(17) Hackett, S. E. J.; Brydson, R. M.; Gass, M. H.; Harvey, I.; Newman, A. D.; Wilson, K.; Lee, A. F. *Angew. Chem., Int. Ed.* **2007**, *46*, 8593.

(18) Parlett, C. M. A.; Bruce, D. W.; Hondow, N. S.; Newton, M. A.; Lee, A. F.; Wilson, K. *ChemCatChem* **2013**, *5*, 939.

(19) Parlett, C. M. A.; Bruce, D. W.; Hondow, N. S.; Lee, A. F.; Wilson, K. *ACS Catal.* **2011**, *1*, 636.

(20) Tsangarakis, C.; Lykakis, I. N.; Stratakis, M. *J. Org. Chem.* **2008**, *73*, 2905.

(21) Fraga, B. M. *Nat. Prod. Rep.* **2012**, *29*, 1334.

(22) Enache, D. I.; Edwards, J. K.; Landon, P.; Solsona-Espriu, B.; Carley, A. F.; Herzing, A. A.; Watanabe, M.; Kiely, C. J.; Knight, D. W.; Hutchings, G. J. *Science* **2006**, *311*, 362.

(23) Nadzri, A. H. A.; Hamzah, N.; Yusoff, N. I. N.; Yarmo, M. A. *Funct. Mater. Lett.* **2011**, *4*, 309.

(24) Dhainaut, J.; Dacquin, J. P.; Lee, A. F.; Wilson, K. *Green Chem.* **2010**, *12*, 296.

(25) Yamaguchi, K.; Mori, K.; Mizugaki, T.; Ebitani, K.; Kaneda, K. *J. Am. Chem. Soc.* **2000**, *122*, 7144.

(26) Mori, K.; Yamaguchi, K.; Mizugaki, T.; Ebitani, K.; Kaneda, K. *Chem. Commun.* **2001**, 461.

(27) Mallat, T.; Baiker, A. *Catal. Today* **1994**, *19*, 247.

(28) Steele, A. M.; Zhu, J.; Tsang, S. C. *Catal. Lett.* **2001**, *73*, 9.

(29) Proch, S.; Herrmannsdorfer, J.; Kempe, R.; Kern, C.; Jess, A.; Seyfarth, L.; Senker, J. *Chem.—Eur. J.* **2008**, *14*, 8204.

(30) Karski, S.; Witonska, I.; Goluchowska, J. *J. Mol. Catal. A: Chem.* **2006**, *245*, 225.

(31) Grunwaldt, J.-D.; Caravati, M.; Baiker, A. *J. Phys. Chem. B* **2006**, *110*, 25586.

(32) Beier, M. J.; Hansen, T. W.; Grunwaldt, J. D. *J. Catal.* **2009**, *266*, 320.

(33) Brett, G. L.; Miedziak, P. J.; Dimitratos, N.; Lopez-Sanchez, J. A.; Dummer, N. F.; Tiruvalam, R.; Kiely, C. J.; Knight, D. W.; Taylor, S. H.; Morgan, D. J.; Carleya, A. F.; Hutchings, G. J. *Catal. Sci. Technol.* **2012**, *2*, 97.

(34) Choudhary, D.; Paul, S.; Rajive, G. A.; Clark, J. H. *Green Chem.* **2006**, *8*, 479.

(35) Hou, Z. S.; Theyssen, N.; Leitner, W. *Green Chem.* **2007**, *9*, 127.

(36) Villa, A.; Wang, D.; Spontoni, P.; Arrigo, R.; Su, D.; Prati, L. *Catal. Today* **2010**, *157*, 89.

(37) Chan-Thaw, C. E.; Villa, A.; Prati, L.; Thomas, A. *Chem.—Eur. J.* **2011**, *17*, 1052.

(38) Zhang, P.; Gong, Y.; Li, H.; Chen, Z.; Wang, Y. *Nat. Commun.* **2013**, *4*, 1593.

(39) Chen, J.; Zhang, Q. H.; Wang, Y.; Wan, H. L. *Adv. Synth. Catal.* **2008**, *350*, 453.

(40) Chen, Y. T.; Guo, Z.; Chen, T.; Yang, Y. H. *J. Catal.* **2010**, *275*, 11.

(41) Yang, P.; Deng, T.; Zhao, D.; Feng, P.; Pine, D.; Chmelka, B. F.; Whitesides, G. M.; Stucky, G. D. *Science* **1998**, *282*, 2244.

(42) Yang, X.-Y.; Leonard, A.; Lemaire, A.; Tian, G.; Su, B.-L. *Chem. Commun.* **2011**, *47*, 2763.

(43) Boissiere, C.; Grosso, D.; Chaumonnot, A.; Nicole, L.; Sanchez, C. *Adv. Mater.* **2010**, *23*, 599.

(44) Chen, X.; Wang, X.; Fu, X. *Energy Environ. Sci.* **2009**, *2*, 872.

(45) Zhang, X.; Hirota, R.; Kubota, T.; Yoneyama, Y.; Tsubaki, N. *Catal. Commun.* **2011**, *13*, 44.

(46) Kamperman, M.; Burns, A.; Weissgraeber, R.; van Vegten, N.; Warren, S. C.; Gruner, S. M.; Baiker, A.; Wiesner, U. *Nano Lett.* **2009**, *9*, 2756.

(47) Lu, S.; Liu, Y.; Wang, Y. *Chem. Commun.* **2010**, *46*, 634.

(48) Woodford, J. J.; Dacquin, J.-P.; Wilson, K.; Lee, A. F. *Energy Environ. Sci.* **2012**, *5*, 6145.

(49) Kamegawa, T.; Suzuki, N.; Che, M.; Yamashita, H. *Langmuir* **2011**, *27*, 2873.

(50) Zhao, D. Y.; Feng, J. L.; Huo, Q. S.; Melosh, N.; Fredrickson, G. H.; Chmelka, B. F.; Stucky, G. D. *Science* **1998**, *279*, 548.

(51) Wainwright, S. G.; Parlett, C. M. A.; Blackley, R. A.; Zhou, W.; Lee, A. F.; Wilson, K.; Bruce, D. W. *Microporous Mesoporous Mater.* **2013**, *172*, 112.

(52) Canton, P.; Menegazzo, F.; Polizzi, S.; Pinna, F.; Pernicone, N.; Riello, P.; Fagherazzi, G. *Catal. Lett.* **2003**, *88*, 141.

(53) Meynen, V.; Cool, P.; Vansant, E. F. *Microporous Mesoporous Mater.* **2009**, *125*, 170.

(54) Wan, Y.; Zhao, D. *Chem. Rev.* **2007**, *107*, 2821.

(55) Gaskell, C. V.; Parlett, C. M. A.; Newton, M. A.; Wilson, K.; Lee, A. F. *ACS Catal.* **2012**, *2*, 2242.

(56) Bowker, M.; Cookson, L.; Bhantoo, J.; Carley, A.; Hayden, E.; Gilbert, L.; Morgan, C.; Counsell, J.; Yaseneva, P. *Appl. Catal., A* **2011**, *391*, 394.